# Gradient Synchronization for Multivariate Functional Data, With Application to Brain Connectivity

Yaqing Chen†
*Department of Statistics, Rutgers University*
Shu-Chin Lin†, Yang Zhou†
*Department of Statistics, University of California, Davis*
Owen Carmichael
*Pennington Biomedical Research Center, Louisiana State University*
Hans-Georg Müller and Jane-Ling Wang‡
*Department of Statistics, University of California, Davis*
for the Alzheimer's Disease Neuroimaging Initiative§

**Summary**. Quantifying the association between components of multivariate random curves is of general interest and is a ubiquitous and basic problem that can be addressed with functional data analysis. An important application is the problem of assessing functional connectivity based on functional magnetic resonance imaging (fMRI), where one aims to determine the similarity of fMRI time courses that are recorded on anatomically separated brain regions. In the functional brain connectivity literature, the static temporal Pearson correlation has been the prevailing measure for functional connectivity. However, recent research has revealed temporally changing patterns of functional connectivity, leading to the study of dynamic functional connectivity. This motivates new similarity measures for pairs of random curves that reflect the dynamic features of functional similarity. Specifically, we introduce gradient synchronization measures in a general setting. These similarity measures are based on the concordance and discordance of the gradients between paired smooth random functions. Asymptotic normality of the proposed estimates is obtained under regularity conditions. We illustrate the proposed synchronization measures via simulations and an application to resting state fMRI signals from the Alzheimer's Disease Neuroimaging Initiative (ADNI) and they are found to improve discrimination between subjects with different disease status.

*Keywords*: Alzheimer's disease; Concordance; fMRI; Functional data analysis; Functional connectivity; Pearson correlation.

†indicates equal contribution
‡Corresponding author, e-mail: janelwang@ucdavis.edu
§Data used in preparation of this article were obtained from the Alzheimer's Disease Neuroimaging Initiative (ADNI) database (`adni.loni.usc.edu`). As such, the investigators within the ADNI contributed to the design and implementation of ADNI and/or provided data but did not participate in analysis or writing of this report. A complete listing of ADNI investigators can be found at: `http://adni.loni.usc.edu/wp-conten/uploads/how_to_apply/ADNI_Acknowledgement_List.pdf`

## 1. Introduction

In many applications, data are collected in the form of curves or signals over time. In the context of functional data analysis (FDA), such curve data are modeled as realizations of an underlying smooth stochastic process. Although a variety of approaches have been proposed for univariate functional data (Ramsay and Dalzell, 1991; Hoover et al., 1998; Fan and Zhang, 1999; Huang et al., 2002; Cardot et al., 2003; Yao et al., 2005; Hall and Horowitz, 2007; Crambes et al., 2009; Shin, 2009; Cai and Yuan, 2012; Chiou and Müller, 2014; Zhu et al., 2014; Chiou et al., 2016), the statistical modeling of dependency between the components of multivariate functional data has received less attention.

Generally, a problem of continuing interest in functional data analysis is the construction of measures of correlation and association between components of multivariate random curves (He et al., 2000). A classical correlation measure is the Pearson product-moment correlation coefficient (PC) (Pearson, 1895) which describes the linear dependence between two random variables. It can be viewed as the cosine of the angle between two centered vectors of a sample. The notion of an angle has been extended to random functions in a Hilbert space (Dubin and Müller, 2005), providing a theoretically supported dynamic functional correlation. A traditional approach to describe the correlation between random vectors is canonical correlation (Hotelling, 1936), which has been extended to multivariate time series (Brillinger, 1975) under the stationarity assumption and to bivariate functional data (Leurgans et al., 1993) under the rubric functional canonical correlation. Functional canonical correlation requires delicate regularization as it involves inverse operators (He et al., 2003; Cupidon et al., 2008; Eubank and Hsing, 2008; He et al., 2004). To avoid the inverse problem, several alternative notions of functional correlation have been proposed, including dynamic correlation (Dubin and Müller, 2005), which is an extension of Pearson correlation to the case of functional data, as it quantifies the angle between random functions, and also a functional correlation based on functional singular decomposition (Yang et al., 2011).

Measures of functional correlation and association are at the core of the quantitative analysis of functional connectivity in neuroscience for time course data obtained from functional magnetic resonance imaging (fMRI). The fMRI time courses are referred to as blood oxygenation level dependent (BOLD) signals, where an increase in blood flow caused by neuronal activity is thought to lead to a surplus in local blood oxygen (Poldrack et al., 2011), and one measures local changes in deoxyhemoglobin concentration in the brain, which serves as a proxy for neural activity (Lindquist, 2008). Functional connectivity as used in neuroimaging corresponds to the temporal correlation of a neurophysiological index measured in different brain areas (Friston et al., 1993). The temporal PC was first applied in resting state fMRI functional connectivity studies by Biswal et al. (1995) and remains one of the predominant tools to measure temporal correlation in the fMRI literature. Other commonly used measures include coherence (Sun et al., 2004; Ombao et al., 2008), which goes back to Wiener (1930), and partial coherence (Tick, 1963) to evaluate the linear relationship between fMRI time series in the frequency domain under various versions of stationarity. Resting state fMRI is a common method to study brain functional connectivity when subjects are not performing an explicit task (Greicius et al., 2003; Shehzad et al., 2009; Biswal, 2012).

As the temporal variability of signals may exhibit changes across time during the

period of data collection, it is of interest to study association measures that can reflect the dynamic characteristics of time courses, especially as the study of variability of connectivity over time has become more popular in recent years (Chang and Glover, 2010; Hutchison et al., 2013; Allen et al., 2014; Lindquist et al., 2014; Patel et al., 2006; Xue et al., 2015), leading to novel approaches to measure functional connectivity in the context of brain diseases such as Alzheimer's disease (van den Heuvel and Pol, 2010; Bijsterbosch et al., 2017). This motivated us to study the application of the proposed measures of synchronization to resting state fMRI signals from Alzheimer's patients. While we highlight fMRI signals as a major application area, the relevance and impact of the proposed methodology is not limited to this specific application. Indeed, Leurgans et al. (1993) and Dubin and Müller (2005) demonstrated how their respective versions of functional correlation led to new insights for the gait data (Ramsay and Silverman, 2005) and multivariate physiological data in nephrology (Kaysen et al., 2000), respectively, in addition to applications to longitudinal medical studies such as the Baltimore Longitudinal Study of Aging (Yang et al., 2011).

To study association in the presence of complex time variability we propose new association measures for paired functional data that emphasize dynamics and are shown to be useful for assessing fMRI based brain connectivity. The proposed measures differ in essential ways from the commonly-used sliding window method (Chang and Glover, 2010) for the analysis of functional connectivity, where one computes temporal Pearson correlations over sliding windows. The proposed measures include *gradient synchronization* and *gradient synchronization fluctuation* and are based on the sign of the product of the derivatives of the two random functions, which is used to track time dynamic synchronicity between two signals. We show that this concept can be interpreted as a limit of temporal Pearson correlations that are constructed over sliding windows when the window size shrinks to zero. Gradient synchronization provides a measure of similarity at the individual level which is readily extended to samples by averaging across subjects. A second measure, gradient synchronization fluctuation, is the number of sign changes of the product of the empirical derivatives of the signals and serves as an additional useful measure. Previous measures to describe changing patterns of connectivity include a dynamic connectivity regression algorithm to detect change points in connectivity (Cribben et al., 2012, 2013) and temporal independent component analysis to obtain temporal functional modes (Smith et al., 2012). In an application to fMRI signals from 11 brain regions (Andrews-Hanna et al., 2010), we find that the proposed gradient synchronization is more closely associated with disease status than traditional PC based measures.

The remainder of the paper is organized as follows. We define the concepts of gradient synchronization and gradient synchronization fluctuation and the proposed estimators in Section 2. Theoretical results that include asymptotic normality for the proposed estimators are given in Section 3. Simulation results are presented in Section 4, followed by an application to resting state fMRI data described in Section 5. A discussion follows in Section 6 and the proofs can be found in Section **??** in the supplement.

## 2. Gradient Synchronization

### *2.1. From Segmented Correlation to Gradient Synchronization*

Let $(X, Y)$ be a pair of centered random functions on an interval $D$, assumed to be $[0, 1]$ without loss of generality. We assume that $X$ and $Y$ are both in the Hilbert space $L_2$ endowed with the inner product $\langle X, Y\rangle = \int_D X(t)Y(t)\mathrm{d}t$. Then $\langle X, Y\rangle/(\|X\|\|Y\|)$ may be viewed as the cosine of the angle between $X$ and $Y$, where $\|X\|^2 = \langle X, X\rangle$.

To introduce the proposed time-varying measure of association between pairs of random curves, we first partition $D$ into many small segments and then calculate the cosine of the angles of the two centered curves on each of the segments induced by the partition. Specifically, let $\mathcal{P} = \{A_1, \ldots, A_{K_\mathcal{P}}\}$ be a collection of disjoint intervals of which the union is $[0, 1]$ and $\delta_\mathcal{P} = \max_{1\le k\le K_\mathcal{P}}\{\mu(A_k)\}$, where $\mu$ stands for the Lebesgue measure on $\mathbb{R}$. Given a random curve $X$, the temporally centered curve on $A_k$ is $X(t) - \int_{A_k} X(s)\mathrm{d}s/\mu(A_k)$, for $t \in A_k$, and analogously for $Y$. The cosine of the angle between the centered curves on the segment $A_k$ is then

$$r_{A_k}(X, Y) = \frac{\int_{A_k}\left\{X(t) - \frac{1}{\mu(A_k)}\int_{A_k} X(s)\mathrm{d}s\right\}\left\{Y(t) - \frac{1}{\mu(A_k)}\int_{A_k} Y(s)\mathrm{d}s\right\}\mathrm{d}t}{\sqrt{\left[\int_{A_k}\left\{X(t) - \frac{1}{\mu(A_k)}\int_{A_k} X(s)\mathrm{d}s\right\}^2\mathrm{d}t\right]\left[\int_{A_k}\left\{Y(t) - \frac{1}{\mu(A_k)}\int_{A_k} Y(s)\mathrm{d}s\right\}^2\mathrm{d}t\right]}}. \tag{1}$$

We observe that $r_{A_k}$ is closely connected to the classical Pearson correlation for paired data observed during the time interval $A_k$, which is the customary measure of connectivity in fMRI research. To see this, approximate the integrals in (1) by Riemann sums over a set of $M$ time points, $t_{1k} < t_{2k} < \cdots < t_{Mk}$, in $A_k$. Then the right hand side of (1) is approximately the Pearson correlation of the $M$ data pairs $(X(t_{mk}), Y(t_{mk}))$, $m = 1, \ldots, M$. Thus, for each pair of curves $(X(t), Y(t))$ their similarity or association can be quantified by a sequence of local similarities $r_{A_k}(X, Y)$ that quantify the similarity between $X$ and $Y$ along the time segments $A_k$. This similarity measure is time dynamic and can be characterized by

$$S_{XY,\mathcal{P}}(t) = \sum_{k=1}^{K_\mathcal{P}} r_{A_k}(X, Y)\mathcal{I}_{A_k}(t), \tag{2}$$

where $\mathcal{I}$ is the indicator function.

Under the following standard assumption (A1),

(A1) $X(\cdot)$ and $Y(\cdot)$ are continuously differentiable on $[0, 1]$ almost surely,

one finds that as the partition $\mathcal{P}$ gets finer, $S_{XY,\mathcal{P}}(t)$ converges to the gradient synchronization (GS) function

$$S_{XY}(t) = \mathrm{sign}\{X'(t)Y'(t)\}, \tag{3}$$

where $\mathrm{sign}(u) = -1, 0, 1$, if $u < 0, u = 0, u > 0$, respectively.

THEOREM 1. *Assume (A1). For any $t \in (0, 1)$ with $\mathbb{P}\{X'(t)Y'(t) = 0\} = 0$, $S_{XY,\mathcal{P}}(t)$ converges to $S_{XY}(t)$ almost surely as $\delta_\mathcal{P} \to 0$.*

We refer to $S_{XY}(\cdot)$ as the gradient synchronization function of $X$ and $Y$ since it captures the synchronization of the derivatives or gradients of $X$ and $Y$. This is illustrated in Figure 1 for a realization of the paired random functions $(X, Y)$ generated according to simulations in Section 4. The oscillations of the random functions result in frequent jumps of $S_{XY}(\cdot)$ between the values 0 and 1, motivating a simple summary measure.

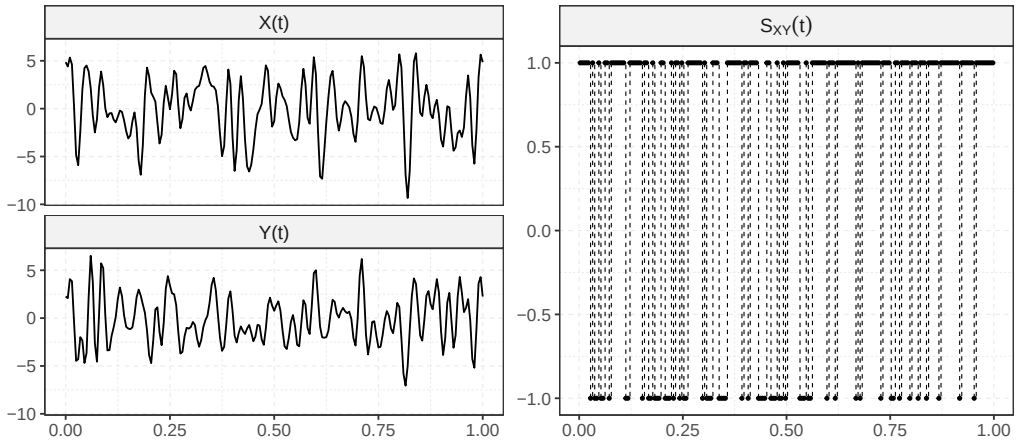


**Fig. 1.** One randomly selected realization of the paired functions $(X(t), Y(t))$ and the corresponding gradient synchronization function $S_{XY}(t)$ (3) generated according to the simulations described in Section 4 with $L = 51$.

Let $\#A$ be the cardinality of a set $A$. For any interval $I \subseteq (0, 1)$, we denote the cardinalities of the random sets of zero crossings for $X'$ and $Y'$ by

$$N_{X'}(I) = \#\{t \in I \mid X'(t) = 0\} \quad \text{and} \quad N_{Y'}(I) = \#\{t \in I \mid Y'(t) = 0\}, \tag{4}$$

respectively, and for $I = (0, 1)$ write $N_{X'} = N_{X'}((0, 1))$ and $N_{Y'} = N_{Y'}((0, 1))$. We need an additional assumption, which is not overly restrictive if (A1) is satisfied.

(A2) Almost surely, $N_{X'}$ and $N_{Y'}$ are finite.

We note that (A2) guarantees that $S_{XY}(\cdot)$ is Riemann integrable almost surely (Theorem 8 in Section 5.3 of Royden and Fitzpatrick, 2010). This leads to

Definition 1. *The gradient synchronization (GS) $R$ and the population GS (pGS) $\rho$ of random functions $X$ and $Y$ are defined as*

$$R = \int_0^1 S_{XY}(t)\mathrm{d}t \quad \textit{and} \quad \rho = \mathbb{E}(R). \tag{5}$$

Obviously, the pGS $\rho$ is always between $-1$ and 1 and is a measure of similarity as the population mean of the aggregated concordance and discordance of the gradients of the random curves $X$ and $Y$. It is positive if both trajectories tend to jointly increase or decrease so that their derivatives have the same sign and is negative if the signals tend to head in opposite directions. With $\rho_+ = \mathbb{E}[\mu\{t \in D : X'(t)Y'(t) > 0\}]$ and $\rho_- = \mathbb{E}[\mu\{t \in D : X'(t)Y'(t) < 0\}]$ representing, respectively, the proportion of the time

domain where concordance and discordance of the derivatives of $X$ and $Y$ occurs, under the assumption that $\mathbb{E}[\mu\{t \in D : X'(t)Y'(t) = 0\}] = 0$, we have $\rho_+ + \rho_- = 1$, whence $\rho_+ = (1+\rho)/2$ and $\rho_- = (1-\rho)/2$ follow in conjunction with $\rho = \rho_+ - \rho_-$. The extreme scenario $\rho = 1$ occurs when $X$ and $Y$ are both monotonically strictly increasing or both monotonically strictly decreasing, and $\rho = -1$ occurs when one of them is monotonically strictly increasing while the other is monotonically strictly decreasing over the entire domain. In all other scenarios one has $-1 < \rho < 1$, where $\rho = 0$ indicates that the aggregated areas of concordance and discordance balance each other out; that is, for half of the time period there is concordance and for the other half there is discordance.

For a simple example, consider two random functions $X(t) = -V\cos(7\pi t/4)$, $Y(t) = V\sin(7\pi t/4)$, $t \in [0,1]$, where $V \sim N(0,1)$. Then

$$\begin{aligned}
\mathbb{E}\left[\int_0^1 \operatorname{sign}\{X'(t)Y'(t)\}\mathrm{d}t\right] &= \int_0^1 \mathbb{E}\left[\operatorname{sign}\{X'(t)Y'(t)\}\right]\mathrm{d}t \\
&= \int_0^1 \mathbb{E}\left[\operatorname{sign}\{(7\pi V/4)^2\sin(7\pi t/2)/2\}\right]\mathrm{d}t \\
&= \int_0^1 \operatorname{sign}\{\sin(7\pi t/2)\}\mathrm{d}t \\
&= \int_0^{2/7} 1\mathrm{d}t - \int_{2/7}^{4/7} 1\mathrm{d}t + \int_{4/7}^{6/7} 1\mathrm{d}t - \int_{6/7}^{1} 1\mathrm{d}t \\
&= 1/7.
\end{aligned}$$

Thus, $\rho = 1/7$ and therefore $\rho_+ = 4/7$ and $\rho_- = 3/7$.

It is also of interest to investigate the expected number of sign changes of $S_{XY}(\cdot)$ from 1 to $-1$ or $-1$ to 1 over time. These sign changes quantify the fluctuation of concordance and discordance between the signals $X$ and $Y$ and thus provide a measure for the stability of gradient synchronization over time. For a piecewise continuous function $f\colon [0,1] \to \mathbb{R}$, denote by $f(t^-) = \lim_{s\to t^-} f(s)$ and $f(t^+) = \lim_{s\to t^+} f(s)$ the left and right limits, respectively. Fluctuations in gradient synchronization can be quantified by counting the sign changes of $S_{XY}(\cdot)$, motivating the following definition of gradient synchronization fluctuation at the population level.

Definition 2. *The gradient synchronization fluctuation (GSF) $Z$ and the population GSF (pGSF) $\zeta$ for random functions $X$ and $Y$ are*

$$Z = \#\{t \in (0,1) \mid S_{XY}(t^-)S_{XY}(t^+) = -1\} \quad \textit{and} \quad \zeta = \mathbb{E}(Z). \tag{6}$$

We note that the GSF $Z$ is finite almost surely since it is bounded by $N_{X'} + N_{Y'}$ which is finite under (A2). To guarantee that $\zeta$ is well defined, we further require the following regularity condition for the cardinalities $N_{X'}$ and $N_{Y'}$ of random sets of zero crossings for $X'$ and $Y'$ as defined in (4).

(A3) $\mathbb{E}(N_{X'}) < \infty$ and $\mathbb{E}(N_{Y'}) < \infty$.

Assumption (A3) requires that the expectations of $N_{X'}$ and $N_{Y'}$ exist and is a stronger condition than (A2). This condition is related to the study of the expected number of

roots of a smooth random function with the Kac-Rice formula (Rice, 1944; Kac, 1948). For a random process $U(\cdot)$ defined on an interval $I$, with $N_U = \#\{t \in I \mid U(t) = 0\}$, these formulas provide certain integrals to calculate $\mathbb{E}(N_U)$ under regularity conditions (Azaïs and Wschebor, 2009; Adler and Taylor, 2009). For a Gaussian random function $U(\cdot)$ taking values in $C^1([0,1])$, a sufficient condition for $\mathbb{E}(N_U) < \infty$ is that the distribution of $U(t)$ is not degenerate for any $t \in [0,1]$ (Azaïs and Wschebor, 2009, Theorem 3.2). An example is given by $U(t) = \sum_{k=1}^{K} A_k \phi_k(t)$, where the $A_k$ are Gaussian random variables and $\{\phi_k(\cdot)\}$ is a polynomial basis or trigonometric basis. Conditions (A2) and (A3) are satisfied if $X$ and $Y$ are Gaussian processes with $C^2([0,1])$ sample paths and $X'(t)$ and $Y'(t)$ are non-degenerate random variables for any $t \in [0,1]$. For non-Gaussian processes, sufficient conditions for $\mathbb{E}(N_U) < \infty$ are in Theorem 3.4 of Azaïs and Wschebor (2009).

### 2.2. Estimation

In practice, data are only available as discrete measurements taken at a grid of time points. For independent copies $\{(X_i, Y_i)\}_{i=1}^n$ of the underlying random processes $(X, Y)$, we assume that $X_i(\cdot)$ and $Y_i(\cdot)$ are observed on $J+1$ time points $0 = t_0 < t_1 < \cdots < t_J = 1$, which form a partition $\mathcal{J} = \{t_j\}_{j=0}^J$ of $[0,1]$. For the $i$th subject, the corresponding GS, as per (5), is given by

$$R_i = \int_0^1 S_{X_i Y_i}(t)\mathrm{d}t = \int_0^1 \mathrm{sign}\{X_i'(t) Y_i'(t)\}\mathrm{d}t. \tag{7}$$

An empirical derivative for $X_i$ and $Y_i$ can be obtained by difference quotients

$$\widehat{X_i'}_{\mathcal{J}}(t) = \sum_{j=1}^{J} D_{j,X_i} \mathcal{I}_{[t_{j-1},t_j)}(t) \quad \text{and} \quad \widehat{Y_i'}_{\mathcal{J}}(t) = \sum_{j=1}^{J} D_{j,Y_i} \mathcal{I}_{[t_{j-1},t_j)}(t), \tag{8}$$

where $D_{j,X_i} = \{X_i(t_j) - X_i(t_{j-1})\}/(t_j - t_{j-1})$, and $D_{j,Y_i}$ is defined analogously. Then a plug-in estimate for $R_i$ is

$$\widehat{R}_{\mathcal{J},i} = \sum_{j=1}^{J} (t_j - t_{j-1}) \mathrm{sign}(D_{j,X_i} D_{j,Y_i}). \tag{9}$$

Naturally, the empirical estimate for the pGS $\rho$ is then

$$\widehat{\rho}_{\mathcal{J}} = \frac{1}{n} \sum_{i=1}^{n} \widehat{R}_{\mathcal{J},i}. \tag{10}$$

The asymptotic normality of the estimate $\widehat{\rho}_{\mathcal{J}}$ is provided in Theorem 2 in Section 3.

For $i = 1, \ldots, n$, as per (6), the subject-specific GSF $Z_i$ is

$$Z_i = \#\{t \in (0,1) \mid S_{X_i Y_i}(t^-) S_{X_i Y_i}(t^+) = -1\}. \tag{11}$$

Since the observable time grid $\mathcal{J} = \{t_j\}_{j=0}^J$ is often pre-determined by a measurement device or sampling plan, a variant of the pGSF $\zeta$ (6) that reflects the time grid $\mathcal{J}$ is also useful. Specifically, a grid-dependent variant $\zeta_{\mathcal{J}}$ of the pGSF is defined as

$$\zeta_{\mathcal{J}} = \mathbb{E}(\widehat{Z}_{\mathcal{J},i}), \tag{12}$$

where $\widehat{Z}_{\mathcal{J},i}$ is an estimate for $Z_i$ by simply counting the sign changes in terms of whether adjacent intervals have the same or different signs of the empirical gradients, i.e.,

$$\begin{aligned}\widehat{Z}_{\mathcal{J},i} = &\#\{2 \le j \le J \mid D_{j-1,X_i} D_{j,X_i} D_{j-1,Y_i} D_{j,Y_i} < 0\} \\ &+ \#\{1 \le j \le J \mid D_{j,X_i} D_{j,Y_i} = 0\},\end{aligned} \tag{13}$$

where $D_{j,X_i}$ and $D_{j,Y_i}$ are defined as after (8). Hence, a sample estimate of $\zeta$ can be obtained by

$$\widehat{\zeta}_{\mathcal{J}} = \frac{1}{n} \sum_{i=1}^{n} \widehat{Z}_{\mathcal{J},i}. \tag{14}$$

We establish the asymptotic normality of $\widehat{\zeta}_{\mathcal{J}}$ in Theorem 3 below, where we consider the pGSF $\zeta$ (6) and the grid-dependent variant $\zeta_{\mathcal{J}}$ (12) as the targets, respectively.

## 3. Asymptotic Properties

For the partition $\mathcal{J}$ of $[0,1]$, let $\delta_{\mathcal{J}} = \max_{1 \le j \le J}\{t_j - t_{j-1}\}$. To derive the asymptotic properties of the proposed estimators, we assume $\delta_{\mathcal{J}} \to 0$ as $n \to \infty$, which requires the grid to get denser as the sample size increases. Although the partition $\mathcal{J} = \mathcal{J}_n$ depends on the sample size $n$, we keep the notation $\mathcal{J}$ instead of $\mathcal{J}_n$ if no confusion arises. Based on assumptions (A1)–(A3), we obtain the consistency and asymptotic normality of $\widehat{\rho}_{\mathcal{J}}$.

THEOREM 2. *(a) If (A1) and (A2) hold, then $\widehat{\rho}_{\mathcal{J}}$ converges to $\rho$ (5) in probability.*

*(b) If (A1) and (A3) hold and $\delta_{\mathcal{J}} = o(n^{-1/2})$, then $\sqrt{n}(\widehat{\rho}_{\mathcal{J}} - \rho)/\widehat{\sigma}_{R,\mathcal{J}}$ converges in distribution to $N(0,1)$, where $\widehat{\sigma}_{R,\mathcal{J}}$ is the square root of the empirical estimate of the variance of $R$, i.e., $\widehat{\sigma}_{R,\mathcal{J}} = \{(n-1)^{-1} \sum_{i=1}^{n} (\widehat{R}_{\mathcal{J},i} - \widehat{\rho}_{\mathcal{J}})^2\}^{1/2}$.*

To obtain the asymptotic normality of $\widehat{\zeta}_{\mathcal{J}}$, we need the following conditions.

(A4) $\mathbb{E}(N_{X'}^2) < \infty$ and $\mathbb{E}(N_{Y'}^2) < \infty$.

(A5) $\mathbb{P}\big(\exists t \in (0,1)$ such that $X'(t) = Y'(t) = 0\big) = 0$.

(A6) There exist constants $C > 0$ and $\epsilon > 0$ such that for all $\delta_{\mathcal{J}} < \epsilon$, the following holds: (1) $\mathbb{P}(N_{X'}(I) = k) \le C|I|^k$ and $\mathbb{P}\big(N_{Y'}(I_j) = k\big) \le C|I|^k$, for all $k \in \mathbb{N}$ and $I \in \{[t_0, t_1), [t_{J-1}, t_J]\}$, as well as for all $k \in \mathbb{N} \cap [2, \infty)$ and $I \in \{[t_{j-2}, t_j) : j = 2, \ldots, J\}$; (2) $\mathbb{P}(N_{X'}(I) = 1, N_{Y'}(I) = 1) \le C|I|^2$, for $I \in \{[t_0, t_1), [t_{J-1}, t_J]\}$. Here $N_{X'}(I)$ and $N_{Y'}(I)$ are defined in (4), and $|I|$ denotes the length of $I$.

Assumption (A4) is needed to obtain the asymptotic normality of $\widehat{\zeta}_{\mathcal{J}}$ when the target is the grid-dependent $\zeta_{\mathcal{J}}$ (12). It is a stronger condition than (A3). Fortunately, we can tap into known results on the second moments of $N_U$ for a random process $U(\cdot)$. For a Gaussian random function $U(\cdot)$ in $C^1([0,1])$, $\mathbb{E}(N_U^2) < \infty$ holds if the joint distribution of $(U(s), U(t))$ is non-degenerate for any $0 \le s < t \le 1$, see Theorem 3.2 of Azaïs and Wschebor (2009). Thus, a sufficient condition for (A4) is that $X$ is a Gaussian process having $C^2([0,1])$ sample paths and the joint distribution $(X'(s), X'(t))$ is non-degenerate

for any $0 \leq s < t \leq 1$ and analogously for $Y$; for non-Gaussian processes see Theorem 3.4 of Azaïs and Wschebor (2009) and chapter 11 of Adler and Taylor (2009).

Assumptions (A5) and (A6) are needed to obtain the asymptotic normality of $\widehat{\zeta}_{\mathcal{J}}$ when targeting the grid-independent pGSF $\zeta$ (6). Specifically, (A5) implies that $X'$ and $Y'$ cannot be zero at the same $t$ almost surely; it does not preclude that there are times $t$ where $X'$ or $Y'$ are zero. This assumption guarantees that $\widehat{Z}_{\mathcal{J},i}$ converges almost surely as $\delta_{\mathcal{J}} \to 0$ and it holds under some regularity conditions as discussed in chapter 3 of Azaïs and Wschebor (2009). In particular, (A5) holds if $(X, Y)$ is a bivariate Gaussian process with $C^2([0,1])$ sample paths and $X'(t)$ and $Y'(t)$ are non-degenerate random variables for any $t \in [0,1]$. Assumption (A6) is a restriction on the frequency of zero crossings of $X'$ and $Y'$, which implies (A4), and is needed to ensure $\zeta_{\mathcal{J}} - \zeta = O(\delta_{\mathcal{J}})$ as $\delta_{\mathcal{J}} \to 0$. Assumption (A6) is satisfied, for example, in the case where $X$ and $Y$ are random polynomials such that the distance between any two zero crossings of $X'$ and $Y'$ is at least $\varepsilon$, where $\varepsilon > 0$ is a constant.

THEOREM 3. *(a) If (A1) and (A4) hold, then* $\sqrt{n}(\widehat{\zeta}_{\mathcal{J}} - \zeta_{\mathcal{J}})/\widehat{\sigma}_{Z,\mathcal{J}}$ *converges in distribution to* $N(0,1)$*, where* $\widehat{\sigma}_{Z,\mathcal{J}}$ *is the square root of the empirical estimate of the variance of* $Z$*, i.e.,* $\widehat{\sigma}_{Z,\mathcal{J}} = \{(n-1)^{-1}\sum_{i=1}^{n}(\widehat{Z}_{\mathcal{J},i} - \widehat{\zeta}_{\mathcal{J}})^2\}^{1/2}$.

*(b) If (A1), (A5) and (A6) hold and* $\delta_{\mathcal{J}} = o(n^{-1/2})$*, then* $\sqrt{n}(\widehat{\zeta}_{\mathcal{J}} - \zeta)/\widehat{\sigma}_{Z,\mathcal{J}}$ *converges in distribution to* $N(0,1)$.

The asymptotic normality of $\widehat{\rho}_{\mathcal{J}}$ and $\widehat{\zeta}_{\mathcal{J}}$ can be utilized for inference such as the construction of asymptotic confidence intervals for $\rho$ and $\zeta$. Let $z_\alpha$ denote the upper $\alpha$-quantile of $N(0,1)$, i.e., $\mathbb{P}(V > z_\alpha) = \alpha$ where $V \sim N(0,1)$. By Theorems 2 and 3, $\widehat{\rho}_{\mathcal{J}} \pm z_{\alpha/2}\widehat{\sigma}_{R,\mathcal{J}}/\sqrt{n}$ and $\widehat{\zeta}_{\mathcal{J}} \pm z_{\alpha/2}\widehat{\sigma}_{Z,\mathcal{J}}/\sqrt{n}$ are $100(1-\alpha)\%$ asymptotic confidence intervals for the pGS $\rho$ and the pGSF $\zeta$.

## 4. Simulation Studies

To demonstrate the finite sample performance of the proposed estimators, our simulation design included $M = 1000$ simulation runs and $n = 50$, 200, and 1000 independent and identically distributed (i.i.d.) pairs of random functions $(X_i, Y_i)$, $i = 1, \ldots, n$. The grid points $\{0 = t_0 < \cdots < t_J = 1\}$ were located equidistantly on $[0,1]$, with the number of grid points chosen as $J = 100$, 200, and 500. Paired functional data $(X_i, Y_i)$ were generated from the trigonometric basis as follows

$$X_i(t_j) = \sum_{l=1}^{L} A_{i,l}\phi_l(t_j) \quad \text{and} \quad Y_i(t_j) = \sum_{l=1}^{L} B_{i,l}\phi_l(t_j),$$

where $L = 91$, $\phi_1(t) \equiv 1$, $\phi_l(t) = \sqrt{2}\cos((l-1)\pi t)$ for odd $l > 1$ and $\phi_l(t) = \sqrt{2}\sin(l\pi t)$ for even $l$, $A_i = (A_{i,1}, \ldots, A_{i,L})^\top$ are i.i.d. random vectors from $N(0, D)$ with the covariance matrix $D$ a diagonal matrix with elements $D_{ll} = \exp(-|l-35|/50)/8$ for $l = 1, \ldots, L$ and $B_i = (B_{i,1}, \ldots, B_{i,L})^\top = aA_i + VC_i$, with $C_i$ independent copies of $A_i$, $V$ an $L \times L$ matrix with $(i,j)$-th entry $V_{ij} = 0.8 \times 0.3^{|i-j|}$, and $a$ such that

$\int_0^1 \mathrm{Var}\{X_i(t)\}\mathrm{d}t = \int_0^1 \mathrm{Var}\{Y_i(t)\}\mathrm{d}t$, i.e. $\sum_{l=1}^L D_{ll} = a^2 \sum_{l=1}^L D_{ll} + \mathrm{trace}(VDV^\top)$, whence $a = 0.48414$. The value of pGS is $\rho = 0.34253$, obtained numerically by averaging the values for $10^6$ paired random functions, recorded on a regular grid with increment $10^{-6}$ on $[0, 1]$. Similarly, the value of pGSF is $\zeta = 130.67$ and its grid-dependent variant $\zeta_{\mathcal{J}}$ equals 42.567, 77.472, and 107.67 for $J = 100$, 200, and 500, respectively, where $J$ determines the segmentation scheme.

Table 1 contains the numerical results for the estimates of pGS and Table 4 the coverage rate of the 95% confidence interval $\widehat{\rho}_{\mathcal{J}} \pm z_{0.025}\widehat{\sigma}_{R,\mathcal{J}}/\sqrt{n}$. We find that the proposed estimator $\widehat{\rho}_{\mathcal{J}}$ converges to the true target $\rho$ as sample size $n$ increases and the coverage rate of the confidence interval is close to the nominal level 95%. The corresponding results for the estimate of pGSF are in Tables 2 and 3, where the target is the grid-dependent variant $\zeta_{\mathcal{J}}$. It can be seen that $\widehat{\zeta}_{\mathcal{J}}$ moves closer to $\zeta_{\mathcal{J}}$ for increasing sample size and the coverage of the confidence intervals is satisfactory.

**Table 1.** Based on $M = 1000$ simulation runs, the first row provides the bias $\mathrm{Bias}(\widehat{\rho}_{\mathcal{J}}) = \sum_{m=1}^M (\widehat{\rho}_{\mathcal{J}}^{[m]} - \rho)/M$, where $\widehat{\rho}_{\mathcal{J}}^{[m]}$ is the proposed estimator of the pGS $\rho$ for the $m$th simulation run. The second row provides the variance $\mathrm{Var}(\widehat{\rho}_{\mathcal{J}}) = \sum_{m=1}^M (\widehat{\rho}_{\mathcal{J}}^{[m]} - M^{-1}\sum_{m'=1}^M \widehat{\rho}_{\mathcal{J}}^{[m']})^2/M$ of the proposed estimator. The third row shows the mean squared error $\mathrm{MSE}(\widehat{\rho}_{\mathcal{J}}) = \sum_{m=1}^M (\widehat{\rho}_{\mathcal{J}}^{[m]} - \rho)^2/M$. All values in the table have been divided by $10^{-4}$.

| | | $J = 100$ | $J = 200$ | $J = 500$ |
|---|---|---|---|---|
| $\mathrm{Bias}(\widehat{\rho}_{\mathcal{J}})$ | $n = 50$ | 11.714 | 4.832 | 3.620 |
| | $n = 200$ | 7.710 | 2.067 | 2.944 |
| | $n = 1000$ | 7.088 | 0.732 | 0.952 |
| $\mathrm{Var}(\widehat{\rho}_{\mathcal{J}})$ | $n = 50$ | 2.059 | 1.730 | 1.556 |
| | $n = 200$ | 0.481 | 0.415 | 0.363 |
| | $n = 1000$ | 0.102 | 0.084 | 0.076 |
| $\mathrm{MSE}(\widehat{\rho}_{\mathcal{J}})$ | $n = 50$ | 2.073 | 1.732 | 1.557 |
| | $n = 200$ | 0.487 | 0.415 | 0.364 |
| | $n = 1000$ | 0.107 | 0.084 | 0.076 |

Often the observable time grid $\mathcal{J}$ is pre-determined by the measurement device and the fluctuation of the gradient synchronization inside intervals $(t_{j-1}, t_j)$ is not detectable. This leads to a natural bias so that $\widehat{\zeta}_{\mathcal{J}}$ underestimates the grid-independent pGSF $\zeta$ in general. We demonstrate this phenomenon in simulations. Table 5 provides the bias, variance and mean squared error of the proposed estimator $\widehat{\zeta}_{\mathcal{J}}$ with respect to the target $\zeta$. The bias decreases as the partition gets finer and the estimating error is seen to be dominated by the bias. Bias correction will be a relevant topic for future research.

In addition, we evaluated the performance of the proposed estimators of pGS and pGSF obtained from samples of smaller size starting from $n = 1$ for functions observed on various time grids with different numbers of time points $J \in \{100, 200, 500\}$. As shown in the boxplots for estimated pGS and pGSF in Figure **??** and **??** in Section **??** in the supplement, for sample sizes $n$ as small as 25, the estimation accuracy is quite

satisfactory.

**Table 2.** Based on $M = 1000$ simulation runs, the first row provides the bias $\mathrm{Bias}_{\mathcal{J}}(\widehat{\zeta}_{\mathcal{J}}) = \sum_{m=1}^{M}(\widehat{\zeta}_{\mathcal{J}}^{[m]} - \zeta_{\mathcal{J}})/M$, where $\widehat{\zeta}_{\mathcal{J}}^{[m]}$ is the proposed estimator of $\zeta$ for the $m$th simulation run. The second row provides the variance $\mathrm{Var}(\widehat{\zeta}_{\mathcal{J}}) = \sum_{m=1}^{M}(\widehat{\zeta}_{\mathcal{J}}^{[m]} - \bar{\zeta}_{\mathcal{J}})^2/M$ of the proposed estimator, where $\bar{\zeta}_{\mathcal{J}} = \sum_{m=1}^{M}\widehat{\zeta}_{\mathcal{J}}^{[m]}/M$. The third row shows the mean squared error $\mathrm{MSE}_{\mathcal{J}}(\widehat{\zeta}_{\mathcal{J}}) = \sum_{m=1}^{M}(\widehat{\zeta}_{\mathcal{J}}^{[m]} - \zeta_{\mathcal{J}})^2/M$.

| | | $J = 100$ | $J = 200$ | $J = 500$ |
|---|---|---|---|---|
| $\mathrm{Bias}_{\mathcal{J}}(\widehat{\zeta}_{\mathcal{J}})$ | $n = 50$ | $-0.023$ | $-0.013$ | $-0.057$ |
| | $n = 200$ | $-0.013$ | $0.011$ | $-0.042$ |
| | $n = 1000$ | $-0.009$ | $0.005$ | $-0.025$ |
| $\mathrm{Var}(\widehat{\zeta}_{\mathcal{J}})$ | $n = 50$ | $0.660$ | $1.468$ | $1.222$ |
| | $n = 200$ | $0.158$ | $0.342$ | $0.300$ |
| | $n = 1000$ | $0.030$ | $0.067$ | $0.059$ |
| $\mathrm{MSE}(\widehat{\zeta}_{\mathcal{J}})$ | $n = 50$ | $0.660$ | $1.468$ | $1.225$ |
| | $n = 200$ | $0.159$ | $0.342$ | $0.302$ |
| | $n = 1000$ | $0.030$ | $0.067$ | $0.060$ |

**Table 3.** Coverage rates for the 95% confidence intervals $\widehat{\zeta}_{\mathcal{J}} \pm z_{0.025}\widehat{\sigma}_{Z,\mathcal{J}}/\sqrt{n}$.

| | $J = 100$ | $J = 200$ | $J = 500$ |
|---|---|---|---|
| $n = 50$ | 0.936 | 0.932 | 0.942 |
| $n = 200$ | 0.953 | 0.950 | 0.949 |
| $n = 1000$ | 0.956 | 0.957 | 0.948 |

As in reality data may be noisy, in addition we considered scenarios where the simulated curves are contaminated with different levels of random noise. To study the case of error contaminated data, we generated the observations of $X_i$ and $Y_i$ as

$$X_{ij} = X_i(t_j) + \epsilon_{ij} \quad \text{and} \quad Y_{ij} = Y_i(t_j) + \varepsilon_{ij},$$

where $\epsilon_{ij}$ and $\varepsilon_{ij}$ for $i = 1, \ldots, n$ and $j = 1, \ldots, J$ are i.i.d. random noise generated from $N(0, \sigma^2_{\mathrm{err},X})$ and $N(0, \sigma^2_{\mathrm{err},Y})$, respectively. We define the signal-to-noise ratio (SNR) as the integrated variance of the random functions divided by the noise variance, i.e.,

$$\mathrm{SNR} = \sqrt{\frac{\int_0^1 \mathrm{Var}\{X_i(t)\}\mathrm{d}t}{\sigma^2_{\mathrm{err},X}}}$$

for functions $X$ and analogously for functions $Y$.

This definition quantifies the contrast of the variability of signal and noise and is also commonly used in fMRI analyses (Stephan et al., 2008; Welvaert and Rosseel, 2013;

Frässle et al., 2017), which is sometimes referred to as contrast-to-noise ratio alternatively. The signal-to-noise ratios considered were 20, 5, and 2, similar to the values taken in simulations of fMRI studies and corresponding to three levels of contamination in the observed data, which in what follows are referred to as low-, medium-, and high-contamination scenarios, respectively. We also compared the estimation of pGS and pGSF based on raw noisy data with the estimation based on band-pass filtered data. For the latter, the band-pass filtering was applied to only preserve frequency components between 0.01 and 0.1 Hz assuming that the recording for an entire function takes 600 seconds, mimicing the Alzheimer's Disease Neuroimaging Initiative (ADNI) fMRI data in Section 5 with around 200 measurements per scan recorded with repetition time (TR) 3000 ms. As shown in Tables **??**–**??** in Section **??** in the supplement, pGS and pGSF are not well estimated based on unfiltered noisy data, especially when the observed time grid $\mathcal{J}$ is relatively dense (e.g., $J = 200$ and $J = 500$). Yet for the band-pass filtered data, the performance of the proposed estimators is found to be much better—both the size of bias and variance shrink overall and the shrinkage is more remarkable as the observed time grid $\mathcal{J}$ gets denser.

**Table 4.** Coverage rates for 95% confidence intervals $\widehat{\rho}_{\mathcal{J}} \pm z_{0.025}\widehat{\sigma}_{R,\mathcal{J}}/\sqrt{n}$.

| | $J = 100$ | $J = 200$ | $J = 500$ |
|---|---|---|---|
| $n = 50$ | 0.944 | 0.937 | 0.930 |
| $n = 200$ | 0.954 | 0.943 | 0.949 |
| $n = 1000$ | 0.945 | 0.956 | 0.947 |

**Table 5.** Based on $M = 1000$ simulation runs, the first row provides the bias $\mathrm{Bias}(\widehat{\zeta}_{\mathcal{J}}) = \sum_{m=1}^{M}(\widehat{\zeta}_{\mathcal{J}}^{[m]} - \zeta)/M$, where $\widehat{\zeta}_{\mathcal{J}}^{[m]}$ is the proposed estimator obtained for the $m$th simulation run. The second row provides the variance $\mathrm{Var}(\widehat{\zeta}_{\mathcal{J}}) = \sum_{m=1}^{M}(\widehat{\zeta}_{\mathcal{J}}^{[m]} - M^{-1}\sum_{m'=1}^{M}\widehat{\zeta}_{\mathcal{J}}^{[m']}/M)^2/M$ of the proposed estimator. The third row shows the mean squared error $\mathrm{MSE}(\widehat{\zeta}_{\mathcal{J}}) = \sum_{m=1}^{M}(\widehat{\zeta}_{\mathcal{J}}^{[m]} - \zeta)^2/M$.

| | | $J = 100$ | $J = 200$ | $J = 500$ |
|---|---|---|---|---|
| $\mathrm{Bias}(\widehat{\zeta}_{\mathcal{J}})$ | $n = 50$ | −88.130 | −53.215 | −23.060 |
| | $n = 200$ | −88.120 | −53.191 | −23.044 |
| | $n = 1000$ | −88.116 | −53.197 | −23.027 |
| $\mathrm{Var}(\widehat{\zeta}_{\mathcal{J}})$ | $n = 50$ | 0.660 | 1.468 | 1.222 |
| | $n = 200$ | 0.158 | 0.342 | 0.300 |
| | $n = 1000$ | 0.030 | 0.067 | 0.059 |
| $\mathrm{MSE}(\widehat{\zeta}_{\mathcal{J}})$ | $n = 50$ | 7767.515 | 2833.317 | 532.969 |
| | $n = 200$ | 7765.237 | 2829.607 | 531.344 |
| | $n = 1000$ | 7764.427 | 2830.023 | 530.322 |

## 5. Application to Resting State fMRI Data

Resting state fMRI data consisting of blood oxygen-level dependent (BOLD) signals while subjects relax were obtained from the Alzheimer's Disease Neuroimaging Initiative (ADNI) database (http://adni.loni.usc.edu). The ADNI fMRI data have different numbers of temporal volumes and we took those scans that have 197 time points so that the sample size is the largest across different time points. Each subject was assigned to one of six cognitive groups: cognitively normal (CN, 279 subjects), subjective memory concerns (SMC, 24 subjects), early mild cognitive impairment (EMCI, 54 subjects), mild cognitive impairment (MCI, 120 subjects), late mild cognitive impairment (LMCI, 20 subjects), and Alzheimer's disease dementia (AD, 36 subjects). From each subject, we considered their earliest available fMRI scans for those with repeated scans. The BOLD signals are measured with repetition time (TR) 3000 ms.

Preprocessing of the BOLD signals followed standard procedures, including head motion correction, slice-timing correction, coregistration, normalization, and spatial smoothing. The first four time points were removed to eliminate non-equilibrium effects of magnetization. Subsequently, average signals of voxels within each seed region were extracted, where linear detrending and band-pass filtering were performed to account for signal drift and global cerebral spinal fluid and white matter signals, including only frequencies between 0.01 and 0.1 Hz, respectively. These steps were performed in MATLAB using the Statistical Parametric Mapping (SPM12, http://www.fil.ion.ucl.ac.uk/spm) and Resting-State fMRI Data Analysis Toolkit V1.8 (REST1.8, http://restfmri.net/forum/?q=rest).

Our analysis focused on the default network, a set of regions that activate when there is no external stimulus (Shulman et al., 1997; Mazoyer et al., 2001; Raichle et al., 2001). Functional connectivity within the default network has been shown to be deficient in a number of neurological diseases including Alzheimer's (Greicius et al., 2004; Buckner et al., 2008). Our analysis focused on the 11 regions of interest (ROIs) within the default network identified in Andrews-Hanna et al. (2010, Table S1, replicated in Table **??** in Section **??** in the supplement). To quantify the strength of inter-regional functional connectivity, we considered the average signals of spherical seed regions of diameter 8 mm centered at the seed voxels of these regions. This yielded 55 paired combinations for the 11 ROIs. To investigate the differences between cognitive groups, we carried out Kruskal–Wallis tests and two-sample Wilcoxon rank sum tests for the equality of the distributions for connectivity measures. Specifically, we first considered a summary statistic of connectivity measures aggregating all 55 pairs of ROIs, the mean of the absolute values (mean size) of pairwise connectivity measures over all 55 ROI pairs, as a single quantity summarizing the magnitude of average hub connectivity.

We considered three connectivity measures: The proposed GS $R_i$ (7) with an estimate $\widehat{R}_{\mathcal{J},i}$ (9) and the proposed GSF $Z_i$ (11) with an estimate $\widehat{Z}_{\mathcal{J},i}$ (13), based on centered signals, as well as the (static) temporal Pearson correlation (PC), which for the $i$th subject with data $(X_i, Y_i)$ is defined as

$$P_{\mathcal{J},i} = \frac{\sum_{j=1}^{J}\{X_i(t_j) - \bar{X}_i\}\{Y_i(t_j) - \bar{Y}_i\}}{\sqrt{\sum_{j=1}^{J}\{X_i(t_j) - \bar{X}_i\}^2}\sqrt{\sum_{j=1}^{J}\{Y_i(t_j) - \bar{Y}_i\}^2}}, \tag{15}$$

with $\bar{X}_i = J^{-1}\sum_{j=1}^{J} X_i(t_j)$ and $\bar{Y}_i = J^{-1}\sum_{j=1}^{J} Y_i(t_j)$. We note that the temporal Pearson correlation is the standard functional connectivity measure used in brain imaging studies and for our analysis is computed based on all the temporal measurements during the screening session with the first four measurement times discarded, as described above. Results of Kruskal–Wallis tests in Table 6 demonstrate that the proposed measures GS and GSF discriminate the six cognitive groups, whereas no significant difference is found among the six groups for temporal Pearson correlation. Furthermore, when applying two-sample Wilcoxon rank sum tests for each pair of cognitive groups (Table 7), temporal PC does not significantly distinguish between any groups, while all pairs of groups except for the pair (MCI, AD) are significantly distinguished by GS and all are distinguished by GSF except for the pairs (CN, LMCI) and (SMC, MCI). When considering simultaneous pairwise comparisons between the fifteen pairs of formed by the six groups, GSF still significantly discriminates ten pairs of groups and GS fourteen pairs.

**Table 6.** $P$-values of the Kruskal–Wallis tests to compare mean sizes over the 55 pairs of ROIs of (static) temporal PC (15), GS (9) and GSF (13) among the six cognitive groups.

| PC | GS | GSF |
|---|---|---|
| 0.63 | $2.1 \times 10^{-61}$ | $2.3 \times 10^{-36}$ |

**Table 7.** $P$-values of the two-sample Wilcoxon rank sum tests to compare mean sizes over the 55 pairs of ROIs of (static) temporal PC (15), GS (9) and GSF (13) between the six cognitive groups. Significance at level $0.05$ for individual tests is marked by "$^*$" and for multiple comparisons after the Bonferroni correction (i.e., less than $0.05/15 \approx 0.0033$) by "$^{**}$".

| Pair of groups | PC | GS | GSF |
|---|---|---|---|
| (CN, SMC) | 0.65 | $1.3 \times 10^{-12**}$ | $0.021^*$ |
| (CN, EMCI) | 0.22 | $1.1 \times 10^{-23**}$ | $7.0 \times 10^{-22**}$ |
| (CN, MCI) | 0.71 | $1.5 \times 10^{-33**}$ | $0.027^*$ |
| (CN, LMCI) | 0.41 | $3.2 \times 10^{-9**}$ | 0.72 |
| (CN, AD) | 0.43 | $3.0 \times 10^{-16**}$ | $3.3 \times 10^{-19**}$ |
| (SMC, EMCI) | 0.22 | $1.6 \times 10^{-5**}$ | $3.8 \times 10^{-10**}$ |
| (SMC, MCI) | 0.77 | $6.8 \times 10^{-10**}$ | 0.11 |
| (SMC, LMCI) | 0.36 | $3.6 \times 10^{-6**}$ | $0.0012^{**}$ |
| (SMC, AD) | 0.33 | $2.6 \times 10^{-7**}$ | $8.1 \times 10^{-11**}$ |
| (EMCI, MCI) | 0.18 | $1.7 \times 10^{-16**}$ | $1.0 \times 10^{-17**}$ |
| (EMCI, LMCI) | 0.96 | $1.4 \times 10^{-8**}$ | $6.1 \times 10^{-9**}$ |
| (EMCI, AD) | 0.80 | $3.4 \times 10^{-10**}$ | $1.7 \times 10^{-4**}$ |
| (MCI, LMCI) | 0.35 | $9.8 \times 10^{-9**}$ | $0.047^*$ |
| (MCI, AD) | 0.36 | 0.35 | $1.5 \times 10^{-16**}$ |
| (LMCI, AD) | 0.86 | $1.4 \times 10^{-7**}$ | $4.0 \times 10^{-9**}$ |

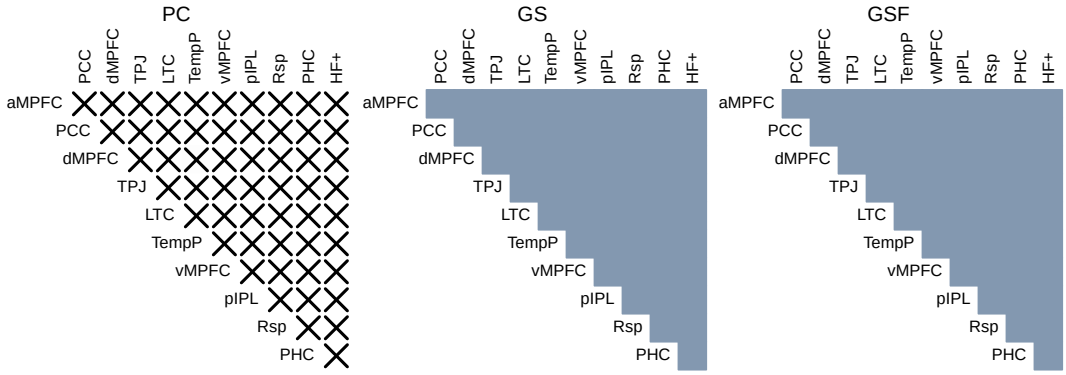


**Fig. 2.** Kruskal–Wallis tests to compare 55 pairs of ROIs simultaneously in terms of (static) temporal PC (15) (left), GS (9) (middle) and GSF (13) (right) among the six cognitive groups, where significance at level 0.05 after Bonferroni adjustment is shown by colored squares and insignificance by crosses.

Another question of interest is whether subjects in different cognitive groups exhibit differences in connectivity among specific pairs of brain regions. To address it, we performed Kruskal–Wallis tests for the 55 combinations of paired ROIs, with comparisons based on temporal Pearson correlation and the proposed GS and GSF. To account for multiple comparisons, $p$-values were adjusted by Bonferroni correction. As illustrated in Figure 2, significant differences among the six cognitive stages were found using GS and GSF for all 55 pairs of ROIs, while no pervasive differences were found when using temporal PC. When employing two-sample Wilcoxon rank sum tests to compare 55 pairs of ROIs simultaneously in terms of (static) temporal PC (15), GS (9) and GSF (13) between subjects in different cognitive groups, again GSF was found to discriminate much better between the various cognitive groups than temporal PC and GS (see Figures **??**–**??** in the supplement).

Beyond static functional connectivity, the proposed synchronicity measures GS and GSF can also be leveraged for the analysis of dynamic functional connectivity. To study the dynamics in resting-state functional connectivity, one of the most commonly used approaches is sliding windows (Hutchison et al., 2013). Specifically, functional connectivity metrics are calculated using data points falling within windows of fixed length that are shifted across the time domain. Accordingly, we compared the performance of the dynamic temporal PC with dynamic counterparts of the proposed GS and GSF.

The dynamic temporal PC of the pair $(X_i, Y_i)$ is defined as

$$P^{\mathrm{dyn}}_{\mathcal{J},i}(s,\Delta) = \frac{\sum_{j=s}^{s+\Delta-1}\{X_i(t_j)-\bar{X}_i(s,\Delta)\}\{Y_i(t_j)-\bar{Y}_i(s,\Delta)\}}{\sqrt{\sum_{j=s}^{s+\Delta-1}\{X_i(t_j)-\bar{X}_i(s,\Delta)\}^2}\sqrt{\sum_{j=s}^{s+\Delta-1}\{Y_i(t_j)-\bar{Y}_i(s,\Delta)\}^2}}, \tag{16}$$

for $s = 1, \ldots, J-\Delta+1$, where $\Delta$ is the window size, $\bar{X}_i(s,\Delta) = \Delta^{-1}\sum_{j=s}^{s+\Delta-1} X_i(t_j)$, and $\bar{Y}_i(s,\Delta) = \Delta^{-1}\sum_{j=s}^{s+\Delta-1} Y_i(t_j)$. The empirical dynamic GS $\widehat{R}^{\mathrm{dyn}}_{\mathcal{J},i}$ and dynamic GSF

$\widehat{Z}^{\mathrm{dyn}}_{\mathcal{J},i}$ can be analogously defined over sliding windows as

$$\begin{aligned}\widehat{R}^{\mathrm{dyn}}_{\mathcal{J},i}(s,\Delta) &= \sum_{j=s}^{s+\Delta-1}(t_j - t_{j-1})\mathrm{sign}(D_{j,X_i}D_{j,Y_i}),\\ \widehat{Z}^{\mathrm{dyn}}_{\mathcal{J},i}(s,\Delta) &= \#\{s+1 \le j \le s+\Delta-1 \mid D_{j-1,X_i}D_{j,X_i}D_{j-1,Y_i}D_{j,Y_i} < 0\}\\ &\quad + \#\{s \le j \le s+\Delta-1 \mid D_{j,X_i}D_{j,Y_i} = 0\},\end{aligned} \tag{17}$$

where $D_{j,X_i}$ and $D_{j,Y_i}$ are defined as after (8). We adopt $\Delta = 15$, which represents measurements during a time interval of 45 seconds and quantify the variability of dynamic functional connectivity for $(X_i, Y_i)$ by the standard deviations of $P^{\mathrm{dyn}}_{\mathcal{J},i}(s,\Delta)$, $\widehat{R}^{\mathrm{dyn}}_{\mathcal{J},i}(s,\Delta)$, and $\widehat{Z}^{\mathrm{dyn}}_{\mathcal{J},i}(s,\Delta)$, over $s \in \{1,\ldots,J-\Delta+1\}$ (Hindriks et al., 2016; Choe et al., 2017).

Based on the averages over the 55 hub pairs of standard deviations of the three dynamic functional connectivity metrics, we performed Kruskal–Wallis tests and two-sample Wilcoxon rank sum tests to compare the various cognitive groups. Significant differences between the six cognitive groups were found for dynamic PC and dynamic GS as well as dynamic GSF (Table 8). Furthermore, dynamic GS and GSF distinguish many more pairs of ROIs than dynamic PC does (Table 9).

**Table 8.** $P$-values of Kruskal–Wallis tests to compare the averages over the 55 pairs of the 11 ROIs in Andrews-Hanna et al. (2010) of standard deviations of dynamic temporal PC (16), GS and GSF (17) among the six cognitive groups.

| dynamic PC | dynamic GS | dynamic GSF |
|---|---|---|
| $1.2 \times 10^{-4}$ | $5.2 \times 10^{-72}$ | $2.0 \times 10^{-60}$ |

We also performed pairwise Kruskal–Wallis tests and two-sample Wilcoxon rank sum tests for all 55 pairs with Bonferroni correction for multiple comparisons and found significant differences in terms of the variability of dynamic GS and GSF between the six cognitive groups, while dynamic PC found none (Figure 3). It emerged that variability of dynamic functional connectivity between many more pairs of ROIs differs significantly between subjects in different cognitive groups in terms of GS and GSF but not for temporal PC (Figures **??**–**??** in the supplement). We repeated this analysis for the 20 ROIs identified by Buckner et al. (2009, Table 4, replicated in Table **??** in Section **??** in the supplement), where similar findings emerged as for the analysis of the 11 ROIs in Andrews-Hanna et al. (2010). Results are provided in Tables **??**–**??** and Figures **??**–**??** in the supplement. In addition, we constructed networks based on the proposed pGS and pGSF; see Section **??** in the supplement.

## 6. Discussion

The proposed new measures, gradient synchronization (GS) and gradient synchronization fluctuation (GSF), measured as integrals and sign changes of $X'(t)Y'(t)$, complement established similarity measures such as Pearson correlation, partial correlation

**Table 9.** $P$-values of two-sample Wilcoxon rank sum tests to compare the averages over the 55 pairs of the 11 ROIs in Andrews-Hanna et al. (2010) of standard deviations of dynamic temporal PC (16), GS and GSF (17) between the six cognitive groups. Significance at level $0.05$ for individual tests is marked by "$^*$" and for multiple comparisons after the Bonferroni correction (i.e. less than $0.05/15 \approx 0.0033$) by "$^{**}$".

| Pair of groups | dynamic PC | dynamic GS | dynamic GSF |
|---|---|---|---|
| (CN, SMC) | 0.50 | $1.1 \times 10^{-12**}$ | $2.0 \times 10^{-13**}$ |
| (CN, EMCI) | $0.042^*$ | $5.3 \times 10^{-25**}$ | $1.4 \times 10^{-21**}$ |
| (CN, MCI) | $0.032^*$ | $3.6 \times 10^{-37**}$ | $1.3 \times 10^{-20**}$ |
| (CN, LMCI) | 0.089 | $5.2 \times 10^{-11**}$ | $4.9 \times 10^{-13**}$ |
| (CN, AD) | $5.5 \times 10^{-6**}$ | $6.8 \times 10^{-22**}$ | $1.1 \times 10^{-20**}$ |
| (SMC, EMCI) | 0.43 | $1.8 \times 10^{-8**}$ | $1.8 \times 10^{-6**}$ |
| (SMC, MCI) | 0.70 | $5.5 \times 10^{-8**}$ | $6.7 \times 10^{-10**}$ |
| (SMC, LMCI) | 0.27 | $3.0 \times 10^{-4**}$ | $2.7 \times 10^{-4**}$ |
| (SMC, AD) | $0.0041^*$ | $5.5 \times 10^{-17**}$ | $2.5 \times 10^{-4**}$ |
| (EMCI, MCI) | 0.70 | $4.3 \times 10^{-16**}$ | $1.4 \times 10^{-14**}$ |
| (EMCI, LMCI) | 0.67 | $7.1 \times 10^{-7**}$ | $1.9 \times 10^{-8**}$ |
| (EMCI, AD) | $0.016^*$ | $3.9 \times 10^{-14**}$ | $6.0 \times 10^{-10**}$ |
| (MCI, LMCI) | 0.57 | $2.6 \times 10^{-6**}$ | $7.1 \times 10^{-11**}$ |
| (MCI, AD) | $0.0021^*$ | $1.9 \times 10^{-19**}$ | $4.5 \times 10^{-17**}$ |
| (LMCI, AD) | 0.20 | $8.8 \times 10^{-10**}$ | $0.011^*$ |

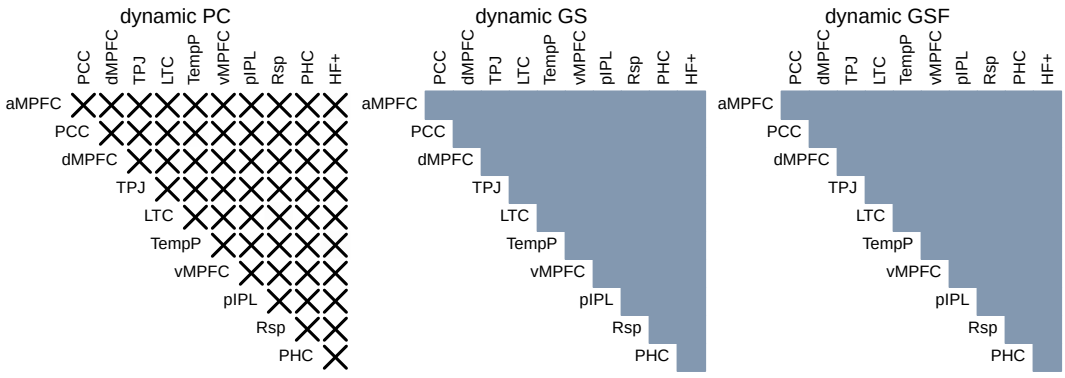


**Fig. 3.** Kruskal–Wallis tests to compare 55 pairs of the 11 ROIs in Andrews-Hanna et al. (2010) simultaneously in terms of the standard deviations of dynamic temporal PC (16) (left), GS (middle) and GSF (right) (17) for the six cognitive groups, where significance at level $0.05$ after Bonferroni adjustment is shown by colored squares and insignificance by crosses.

(e.g., Marrelec et al., 2006), mutual information and partial/conditional mutual information (e.g., Salvador et al., 2005; Gretton et al., 2006; Salvador et al., 2007, 2010; Cassidy et al., 2014). In brain connectivity studies, mutual and partial mutual information are often applied in the frequency domain and hence reflect the dependence/similarity of paired random functions across different frequencies (e.g., Salvador et al., 2005, 2007, 2010; Cassidy et al., 2014), while the proposed measures focus on the similarity of temporal dynamics. Specifically, GS captures the average aggregated concordance and discordance of the change rates between random curves, while GSF provides a complementary measure of the stability of the gradient synchronization.

*Application to fMRI Data.* The proposed measures were found to better distinguish different cognitive groups in the Alzheimer's disease spectrum for the ADNI data compared to standard Pearson correlation (PC) based measures. Reduced connectivity between the posterior cingulate cortex (PCC) and the medial temporal lobe (MTL) structures was previously found for AD patients compared to normal controls (Greicius et al., 2004). Among the eleven regions in the default network identified in Andrews-Hanna et al. (2010), five belong to the MTL subsystem, namely ventral MPFC (vMPFC), posterior inferior parietal lobule (pIPL), retrosplenial cortex (Rsp), parahippocampal cortex (PHC), and hippocampal formation (HF+). In contrast to temporal PC, GSF and variance of dynamic GS were found to significantly differ between PCC and MTL regions among the six groups (Figures 2 and 3) and also between CN and other groups (Figures **??**, **??**, and **??** in the supplement). Reduced metabolism and perfusion in parietal lobes, medial temporal structures and the PCC in Alzheimer's (Matsuda, 2001; Bradley et al., 2002) may also be related to the deficient connectivity between these regions. Reduced connectivity between the temporal parietal junction (TPJ) and the PCC as well as the five MTL regions is partly identified by GSF and more fully by dynamic GS, but not by temporal PC (Figures 2 and 3; Figures **??**, **??**, and **??** in the supplement).

*Consistency, Reliability, and Comparison of Different fMRI Measures.* Following other fMRI studies (e.g., Zhao et al., 2023), we evaluated the individual stability of the proposed GS and GSF as well as temporal PC based on first two consecutive fMRI scans taken from CN subjects such that second scans are taken within 12 months of the first scans. To measure individual stability, we computed the intra-class correlation (ICC) (Shrout and Fleiss, 1979). Considering a set of measures obtained from scan $j$ and subject $i$ for $j = 1, \ldots, k$ and $i = 1, \ldots, n$, denoted by $\{x_{ij}\}$, ICC is defined as

$$\text{ICC} = \frac{\text{BMS} - \text{WMS}}{\text{BMS} + (k-1)\text{WMS}}.$$

Here, $\text{BMS} = \sum_{i=1}^{n} k(\bar{x}_{i\cdot} - \bar{x}_{\cdot\cdot})^2/(n-1)$ and $\text{WMS} = \sum_{i=1}^{n}\sum_{j=1}^{k}(x_{ij} - \bar{x}_{i\cdot})^2/\{n(k-1)\}$, and in our case, $k = 2$. Higher values of ICC imply that variability in the corresponding measure is driven by the variation across subjects to more extent and that the measure is more stable for each subject. We computed ICC for each of the 55 pairs of ROIs in the default network identified in Andrews-Hanna et al. (2010) for each measure, temporal PC (15), GS (9) and GSF (13), respectively. As seen in in Figure 4, the three measures yield similar ICCs and hence have comparable subject stability, while the ICCs of GS

and GSF have higher variation among pairs of ROIs. We repeated the analysis on the 190 pairs of ROIs identified in Buckner et al. (2009, Table 4) and found that subject stability of GSF is as good as that of PC while the subject stability of GS is slightly inferior (Figure 5). Comparing ICCs of different functional connectivity measures evaluated over different sets of ROIs in Figures 4 and 5, we find that, similar to Zhao et al. (2023), within-network individual stability of PC and GS is higher than across-network individual stability, noting that the 11 ROIs identified in Andrews-Hanna et al. (2010) all lie in the default network while the 20 ROIs identified in Buckner et al. (2009, Table 4) fall in multiple networks including the default network. For GSF, both within-network and across-network individual stability are high.

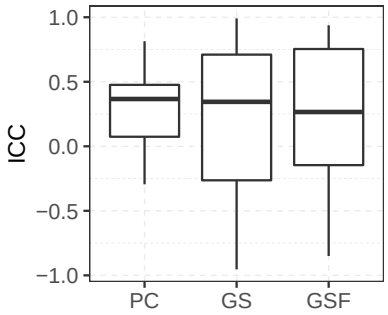


**Fig. 4.** Boxplots of ICCs of temporal PC (15) (left), GS (9) (middle) and GSF (13) (right) evaluated over the 55 pairs of ROIs in the default network identified in Andrews-Hanna et al. (2010, Table S1).

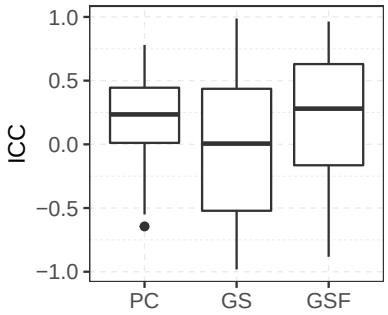


**Fig. 5.** Boxplots of ICCs of temporal PC (15) (left), GS (9) (middle) and GSF (13) (right) evaluated over the 190 pairs of ROIs identified in Buckner et al. (2009, Table 4).

*General Applicability.* While our approach was motivated by a study of functional connectivity of the human brain and we illustrate our methods in this paper with resting state BOLD fMRI signals, the proposed methods are broadly applicable to multivariate functional data. Such data are increasingly encountered, for example in longitudinal studies with densely measured multivariate outcomes. One advantage of the segmen-

tation technique is that it keeps track of local dynamic behavior and both the average behavior as well as the stability of synchronization over time can be quantified and studied. A noteworthy feature is that no smoothing parameter selection is required. By exploiting the functional features of the data, we avoid assumptions of temporal stationarity that have been imposed for signals in fMRI studies. The proposed methods are also suitable to quantify the temporal variability of signals, including changes of synchronization patterns over time, e.g., in task-based fMRI studies.

## Acknowledgements

We thank three referees and the Associate Editor for constructive comments. This research has been supported by NSF grants DMS-2311035 (YC), DMS-1712864, DMS-2014526 (HGM), DMS-1914917 and DMS-2210891 (JLW). Owen Carmichael's research has been supported by NIH grants AG10220, AG10129, AG030514, AG031252, and AG021028. We thank the Alzheimer's Disease Neuroimaging Initiative (NIH grant U01 AG024904, Department of Defense award W81XWH-12-2-0012) for the data access.

## References

Adler, R. J. and Taylor, J. E. (2009) *Random Fields and Geometry*. Springer Science & Business Media.

Allen, E. A., Damaraju, E., Plis, S. M., Erhardt, E. B., Eichele, T. and Calhoun, V. D. (2014) Tracking whole-brain connectivity dynamics in the resting state. *Cerebral Cortex*, **24**, 663–676.

Andrews-Hanna, J. R., Reidler, J. S., Sepulcre, J., Poulin, R. and Buckner, R. L. (2010) Functional-anatomic fractionation of the brain's default network. *Neuron*, **65**, 550–562.

Azaïs, J.-M. and Wschebor, M. (2009) *Level Sets and Extrema of Random Processes and Fields*. John Wiley & Sons.

Bijsterbosch, J., Smith, S. M. and Beckmann, C. F. (2017) *Introduction to resting state fMRI functional connectivity*. Oxford University Press.

Biswal, B., Yetkin, F. Z., Haughton, V. M. and Hyde, J. S. (1995) Functional connectivity in the motor cortex of resting human brain using echo-planar MRI. *Magnetic Resonance in Medicine*, **34**, 537–541.

Biswal, B. B. (2012) Resting state fMRI: A personal history. *Neuroimage*, **62**, 938–944.

Bradley, K., O'sullivan, V., Soper, N., Nagy, Z., King, E.-F., Smith, A. and Shepstone, B. (2002) Cerebral perfusion SPET correlated with braak pathological stage in Alzheimer's disease. *Brain*, **125**, 1772–1781.

Brillinger, D. (1975) *Times Series: Data Analysis and Theory*. New York: SIAM: Society for Industrial and Applied Mathematics. Classics in Applied Mathematics.

Buckner, R. L., Andrews-Hanna, J. R. and Schacter, D. L. (2008) The brain's default network: Anatomy, function, and relevance to disease. *Annals of the New York Academy of Sciences*, **1124**, 1–38.

Buckner, R. L., Sepulcre, J., Talukdar, T., Krienen, F. M., Liu, H., Hedden, T., Andrews-Hanna, J. R., Sperling, R. A. and Johnson, K. A. (2009) Cortical hubs revealed by intrinsic functional connectivity: Mapping, assessment of stability, and relation to Alzheimer's disease. *The Journal of Neuroscience*, **29**, 1860–1873.

Cai, T. and Yuan, M. (2012) Minimax and adaptive prediction for functional linear regression. *Journal of the American Statistical Association*, **107**, 1201–1216.

Cardot, H., Ferraty, F. and Sarda, P. (2003) Spline estimators for the functional linear model. *Statistica Sinica*, **13**, 571–591.

Cassidy, B., Rae, C. and Solo, V. (2014) Brain activity: Connectivity, sparsity, and mutual information. *IEEE Transactions on Medical Imaging*, **34**, 846–860.

Chang, C. and Glover, G. H. (2010) Time-frequency dynamics of resting-state brain connectivity measured with fMRI. *NeuroImage*, **50**, 81–98.

Chiou, J.-M. and Müller, H.-G. (2014) Linear manifold modelling of multivariate functional data. *Journal of the Royal Statistical Society: Series B (Statistical Methodology)*, **76**, 605–626.

Chiou, J.-M., Yang, Y.-F. and Chen, Y.-T. (2016) Multivariate functional linear regression and prediction. *Journal of Multivariate Analysis*, **146**, 301–312.

Choe, A. S., Nebel, M. B., Barber, A. D., Cohen, J. R., Xu, Y., Pekar, J. J., Caffo, B. and Lindquist, M. A. (2017) Comparing test-retest reliability of dynamic functional connectivity methods. *NeuroImage*, **158**, 155–175.

Crambes, C., Kneip, A. and Sarda, P. (2009) Smoothing splines estimators for functional linear regression. *The Annals of Statistics*, **37**, 35–72.

Cribben, I., Haraldsdottir, R., Atlas, L. Y., Wager, T. D. and Lindquist, M. A. (2012) Dynamic connectivity regression: Determining state-related changes in brain connectivity. *NeuroImage*, **61**, 907–920.

Cribben, I., Wager, T. D. and Lindquist, M. A. (2013) Detecting functional connectivity change points for single-subject fMRI data. *Frontiers in Computational Neuroscience*, **7**, 143.

Cupidon, J., Eubank, R., Gilliam, D. and Ruymgaart, F. (2008) Some properties of canonical correlations and variates in infinite dimensions. *Journal of Multivariate Analysis*, **99**, 1083–1104.

Dubin, J. and Müller, H. G. (2005) Dynamical correlation for multivariate longitudinal data. *Journal of the American Statistical Association*, **100**, 872–881.

Eubank, R. L. and Hsing, T. (2008) Canonical correlation for stochastic processes. *Stochastic Processes and their Applications*, **118**, 1634–1661.

Fan, J. and Zhang, W. (1999) Statistical estimation in varying coefficient models. *The Annals of Statistics*, **27**, 1491–1518.

Frässle, S., Lomakina, E. I., Razi, A., Friston, K. J., Buhmann, J. M. and Stephan, K. E. (2017) Regression DCM for fMRI. *NeuroImage*, **155**, 406–421.

Friston, K. J., Frith, C. D., Liddle, P. F. and Frackowiak, R. S. J. (1993) Functional connectivity: the principal-component analysis of large (pet) data sets. *Journal of Cerebral Blood Flow & Metabolism*, **13**, 5–14.

Greicius, M. D., Krasnow, B., Reiss, A. L. and Menon, V. (2003) Functional connectivity in the resting brain: A network analysis of the default mode hypothesis. *Proceedings of the National Academy of Sciences*, **100**, 253–258.

Greicius, M. D., Srivastava, G., Reiss, A. L. and Menon, V. (2004) Default-mode network activity distinguishes Alzheimer's disease from healthy aging: Evidence from functional MRI. *Proceedings of the National Academy of Sciences*, **101**, 4637–4642.

Gretton, A., Belitski, A., Murayama, Y., Schölkopf, B. and Logothetis, N. (2006) The effect of artifacts on dependence measurement in fMRI. *Magnetic Resonance Imaging*, **24**, 401–409.

Hall, P. and Horowitz, J. L. (2007) Methodology and convergence rates for functional linear regression. *The Annals of Statistics*, **35**, 70–91.

He, G., Müller, H.-G. and Wang, J.-L. (2000) Extending correlation and regression from multivariate to functional data. In *Asymptotics in Statistics and Probability*, 197–210. De Gruyter.

He, G., Müller, H. G. and Wang, J.-L. (2003) Functional canonical analysis for square integrable stochastic processes. *Journal of Multivariate Analysis*, **85**, 54–77.

He, G., Müller, H.-G. and Wang, J.-L. (2004) Methods of canonical analysis for functional data. *Journal of Statistical Planning and Inference*, **122**, 141–159.

van den Heuvel, M. P. and Pol, H. E. H. (2010) Exploring the brain network: A review on resting-state fMRI functional connectivity. *European Neuropsychopharmacology*, **20**, 519–534.

Hindriks, R., Adhikari, M. H., Murayama, Y., Ganzetti, M., Mantini, D., Logothetis, N. K. and Deco, G. (2016) Can sliding-window correlations reveal dynamic functional connectivity in resting-state fMRI? *NeuroImage*, **127**, 242–256.

Hoover, D., Rice, J., Wu, C. and Yang, L. (1998) Nonparametric smoothing estimates of time-varying coefficient models with longitudinal data. *Biometrika*, **85**, 809–822.

Hotelling, H. (1936) Relation between two sets of variables. *Biometrika*, **28**, 321–377.

Huang, J., Wu, C. and Zhou, L. (2002) Varying-coefficient models and basis function approximations for the analysis of repeated measurements. *Biometrika*, **89**, 111–128.

Hutchison, R. M., Womelsdorf, T., Allen, E. A., Bandettini, P. A., Calhoun, V. D., Corbetta, M., Penna, S. d., Duyn, J. H., Glover, G. H., Gonzalez-Castillo, J., Handwerker, D. A., Keilholz, S., Kiviniemi, V., Leopold, D. A., de Pasquale, F., Sporns, O., Walter, M. and Chang, C. (2013) Dynamic functional connectivity: Promise, issues, and interpretations. *NeuroImage*, **80**, 360–378.

Kac, M. (1948) On the average number of real roots of a random algebraic equation (II). *Proceedings of the London Mathematical Society*, **2**, 390–408.

Kaysen, G. A., Dubin, J. A., Müller, H.-G., Rosales, L. M. and Levin, N. W. (2000) The acute-phase response varies with time and predicts serum albumin levels in hemodialysis patients. *Kidney International*, **58**, 346–352.

Leurgans, S. E., Moyeed, R. A. and Silverman, B. W. (1993) Canonical correlation analysis when the data are curves. *Journal of the Royal Statistical Society: Series B (Statistical Methodology)*, **55**, 725–740.

Lindquist, M. A. (2008) The statistical analysis of fMRI data. *Statistical Science*, **23**, 439–464.

Lindquist, M. A., Xu, Y., Nebel, M. B. and Caffo, B. S. (2014) Evaluating dynamic bivariate correlations in resting-state fMRI: A comparison study and a new approach. *NeuroImage*, **101**, 531–546.

Marrelec, G., Krainik, A., Duffau, H., Pélégrini-Issac, M., Lehéricy, S., Doyon, J. and Benali, H. (2006) Partial correlation for functional brain interactivity investigation in functional MRI. *Neuroimage*, **32**, 228–237.

Matsuda, H. (2001) Cerebral blood flow and metabolic abnormalities in Alzheimer's disease. *Annals of Nuclear Medicine*, **15**, 85–92.

Mazoyer, B., Zago, L., Mellet, E., Bricogne, S., Etard, O., Houdé, O., Crivello, F., Joliot, M., Petit, L. and Tzourio-Mazoyer, N. (2001) Cortical networks for working memory and executive functions sustain the conscious resting state in man. *Brain Research Bulletin*, **54**, 287–298.

Ombao, H., Shao, X., Rykhlevskaia, E., Fabiani, M. and Gratton, G. (2008) Spatio-spectral analysis of brain signals. *Statistica Sinica*, 1465–1482.

Patel, R. S., Bowman, F. D. and Rilling, J. K. (2006) A Bayesian approach to determining connectivity of the human brain. *Human Brain Mapping*, **27**, 267–276.

Pearson, K. (1895) Notes on regression and inheritance in the case of two parents. *Proceedings of the Royal Society of London*, **58**, 240–242.

Poldrack, R. A., Mumford, J. A. and Nichols, T. E. (2011) *Handbook of Functional MRI Data Analysis*. New York: Cambridge University Press. Classics in Applied Mathematics.

Raichle, M. E., MacLeod, A. M., Snyder, A. Z., Powers, W. J., Gusnard, D. A. and Shulman, G. L. (2001) A default mode of brain function. *Proceedings of the National Academy of Sciences*, **98**, 676–682.

Ramsay, J. O. and Dalzell, C. J. (1991) Tools for functional data analysis. *Journal of the Royal Statistical Society: Series B (Statistical Methodology)*, **53**, 539–572.

Ramsay, J. O. and Silverman, B. W. (2005) *Functional Data Analysis*. New York: Springer, 2nd edn. Springer Series in Statistics.

Rice, S. O. (1944) Mathematical analysis of random noise. *Bell System Technical Journal*, **23**, 282–332.

Royden, H. L. and Fitzpatrick, P. (2010) *Real Analysis*. Pearson Education, Inc., 4th edn.

Salvador, R., Anguera, M., Gomar, J. J., Bullmore, E. T. and Pomarol-Clotet, E. (2010) Conditional mutual information maps as descriptors of net connectivity levels in the brain. *Frontiers in Neuroinformatics*, **4**, 115.

Salvador, R., Martinez, A., Pomarol-Clotet, E., Sarró, S., Suckling, J. and Bullmore, E. (2007) Frequency based mutual information measures between clusters of brain regions in functional magnetic resonance imaging. *NeuroImage*, **35**, 83–88.

Salvador, R., Suckling, J., Schwarzbauer, C. and Bullmore, E. (2005) Undirected graphs of frequency-dependent functional connectivity in whole brain networks. *Philosophical Transactions of the Royal Society B: Biological Sciences*, **360**, 937–946.

Shehzad, Z., Kelly, A. M. C., Reiss, P. T., Gee, D. G., Gotimer, K., Uddin, L. Q., Lee, S. H., Margulies, D. S., Roy, A. K., Biswal, B. B., Petkova, E., Castellanos, F. X. and Milham, M. P. (2009) The resting brain: Unconstrained yet reliable. *Cerebral Cortex*, **19**, 2209–2229.

Shin, H. (2009) Partial functional linear regression. *Journal of Statistical Planning and Inference*, **139**, 3405–3418.

Shrout, P. E. and Fleiss, J. L. (1979) Intraclass correlations: Uses in assessing rater reliability. *Psychological Bulletin*, **86**, 420–428.

Shulman, G., Fiez, J., Corbetta, M., Buckner, R., Miezen, F., Raichle, M. and Petersen, S. (1997) Common blood flow changes across visual tasks: II. Decreases in cerebral cortex. *Journal of Cognitive Neuroscience*, **9**, 648–663.

Smith, S. M., Miller, K. L., Moeller, S., Xu, J., Auerbach, E. J., Woolrich, M. W., Beckmann, C. F., Jenkinson, M., Andersson, J., Glasser, M. F., Van Essen, D. C., Feinberg, D. A., Yacoub, E. S. and Ugurbil, K. (2012) Temporally independent functional modes of spontaneous brain activity. *Proceedings of the National Academy of Sciences*, **109**, 3131–3136.

Stephan, K. E., Kasper, L., Harrison, L. M., Daunizeau, J., den Ouden, H. E., Breakspear, M. and Friston, K. J. (2008) Nonlinear dynamic causal models for fMRI. *NeuroImage*, **42**, 649–662.

Sun, F. T., Miller, L. M. and D'Esposito, M. (2004) Measuring interregional functional connectivity using coherence and partial coherence analyses of fMRI data. *NeuroImage*, **21**, 647–658.

Tick, L. J. (1963) Time series analysis. In *Conditional Spectra, Linear Systems, and Coherency.* (ed. M. Rosenblatt), 197–203. Wiley.

Welvaert, M. and Rosseel, Y. (2013) On the definition of signal-to-noise ratio and contrast-to-noise ratio for fMRI data. *PLoS ONE*, **8**, e77089.

Wiener, N. (1930) Generalised harmonic analysis. *Acta Mathematica*, **55**, 117–258.

Xue, W., Bowman, F. D., Pileggi, A. V. and Mayer, A. R. (2015) A multimodal approach for determining brain networks by jointly modeling functional and structural connectivity. *Frontiers in Computational Neuroscience*, **9**, 22.

Yang, W., Müller, H. G. and Stadtmüller, U. (2011) Functional singular component analysis. *Journal of the Royal Statistical Society: Series B (Statistical Methodology)*, **73**, 303–324.

Yao, F., Müller, H.-G. and Wang, J.-L. (2005) Functional linear regression analysis for longitudinal data. *The Annals of Statistics*, **33**, 2873–2903.

Zhao, B., Li, T., Li, Y., Fan, Z., Xiong, D., Wang, X., Gao, M., Smith, S. M. and Zhu, H. (2023) An atlas of trait associations with resting-state and task-evoked human brain functional organizations in the UK Biobank. *Imaging Neuroscience*, **1**, 1–23.

Zhu, H., Fan, J. and Kong, L. (2014) Spatially varying coefficient model for neuroimaging data with jump discontinuities. *Journal of the American Statistical Association*, **109**, 1084–1098.